J Infrared Milli Terahz Waves (2013) 34:393–404
DOI 10.1007/s10762-013-9978-2

Terahertz LC Microcavities: From Quantum Cascade Lasers to Ultrastrong Light-Matter Coupling

Markus Geiser · Giacomo Scalari · Mattias Beck · Christoph Walther · Jérôme Faist

Received: 6 December 2012 / Accepted: 22 April 2013 /
Published online: 19 May 2013

Abstract We review research on the physics of intersubband transitions in the THz range in a sub wavelength microcavity environment. Laser action was achieved at 1.5 THz by inserting quantum cascade gain material between the capacitor plates of a new resonant LC cavity, achieving a normalized mode volume ratio of only $V_{eff}/(\lambda/2n)^3 = 0.12$ of the cavity mode V_{eff} and the normalized optical volume $(\lambda/2n)^3$. By using the same cavity as the constituting meta-atom of a THz metamaterial, strong and ultra strong light matter coupling was observed up to room temperature. Finally, the same metamaterial coupled to parabolic semiconductor quantum wells was investigated in the regime of electrical in-plane pumping, showing THz emission in the ultra strong coupling regime.

Keywords Microcavity · LC · Electronic feedback · Strong coupling · Ultra strong coupling · Polariton · Intersubband polariton · Purcell effect · Nonresonant pumping · Quantum cascade laser

The physics of solid-state quantum emitters embedded in microcavities has represented an extremely fertile research field in the past 30 years [1, 2]. Light-matter coupling in a microcavity environment opened up new possibilities in many research

M. Geiser (✉) · G. Scalari · M. Beck · C. Walther · J. Faist
Institute for Quantum Electronics, ETH Zurich, Wolfgang- Pauli-Strasse 16, 8093 Zurich, Switzerland
e-mail: mgeiser@ethz.ch

G. Scalari
e-mail: scalari@phys.ethz.ch

J. Faist
e-mail: jerome.faist@phys.ethz.ch

fields, from laser physics to cavity polaritons to on-chip quantum information processing [3]. Since many peculiar cavity effects scale with the inverse of the microcavity volume V [2, 3], there is great interest in realizing a system where the ratio between the cavity volume and the cube of the half-wavelength in the material $V_{eff}/(\lambda/2n)^3$ is as small as possible. Borrowing concepts from electronics, a recent addition to the available resonators in the Terahertz (THz) range is the so called LC-resonator [4]. It functionally resembles an electronic inductance-capacitance (LC) circuit, where energy is stored spatially and temporally separated in a capacitance and an inductance element. This kind of cavity is not limited to a size of $(\lambda/2n)^3$ as dielectric cavities are. Here, λ is the free space wavelength and n is the mode refractive index. Typical examples of dielectric cavities are ridges and microdisks as shown in Fig. 1a with their respective sizes. In the quantum cascade (QC) laser community, strong subwavelength confinement in one direction is widely exploited in the case of metal-metal waveguides [5], while such strong confinement in all three dimensions was not yet demonstrated. The LC-cavity allows for very small mode volumes and is interesting for devices featuring low dissipation and fast modulation as well as a basis for cavity-QED experiments [6–8]. Other circuit-inspired cavities such as metamaterials based on split-ring resonators[9] present deep subwavelength sizes and exhibit strong resonant behavior, making them available for cavity quantum electrodynamics studies in the THz range [10–12]. In this present review, we will first discuss the characteristics of the LC cavity and then cover its applications for lasers and devices in the strong coupling regime in individual sections.

1 LC Resonator

Electromagnetic theory scales from the electronic regime to higher optical frequencies, allowing in principle operation of electronic circuits at THz frequencies when scaled in electrical size. An LC circuit with a THz range resonance frequency $\omega = 1/\sqrt{LC}$ can consist of components of few μm dimensions, accessible by optical lithography fabrication techniques. Such a device is shown schematically in Fig. 1b. The inductance is implemented as a wire which is connected to

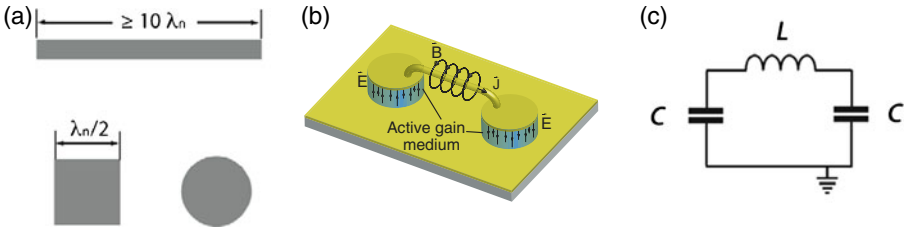

Fig. 1 Cavities as ridges, patch antennas and microdiscs with their typical sizes are shown in (**a**). **b** schematic of an inductance-capacitance circuit: A wire connecting two capacitor plates which are situated above a ground plane. A circuit representation of the cavity is shown in (**c**). The figure is adapted from [4]

a plate at each end. These plates form capacitors with a ground plane. As the resonance frequency of such a device is not dependent on its physical dimension, mode volumes can be lower than in previously demonstrated cavities [13–15]. In laser cavities, an effective Volume of $V_{eff} = 0.12(\lambda/2n)^3$ has been achieved [4]. Polaritonic electroluminescent devices as described below [16] have been realized with a lower mode volume of $V_{eff} = 0.02(\lambda/2n)^3$. Similar resonators with an even lower mode volume of $V_{eff} = 0.0025(\lambda/2n)^3$ have been studied in reflection measurements [12]. The circuit representation of the device is shown in Fig. 1c. Fabricated devices currently rely on planar metallic (typically gold) cavities. The field distribution in such a device was investigated with a commercial finite element simulation package and is plotted in Fig. 2a and b for the electric and magnetic field respectively. Shown is a cut parallel to the ground plane at half the height of the capacitor. The field distribution illustrates the spatial separation of the fields and the functionality of the cavity elements. An electron micrograph of a fabricated device is shown in Fig. 2c. In addition to the cavity, a feeding line for electrical connection is visible. An absorption spectrum of a cavity with 1.45 THz resonance frequency is presented in (d), showing the single mode character of the cavity.

In a LC cavity, it is in principle possible to engineer the device farfield by shaping the inductance element and with it the cavity radiation pattern. This is an advantage over metal metal waveguides, which are suffering from a poor radiation coupling to free space due to strong impedance mismatch.

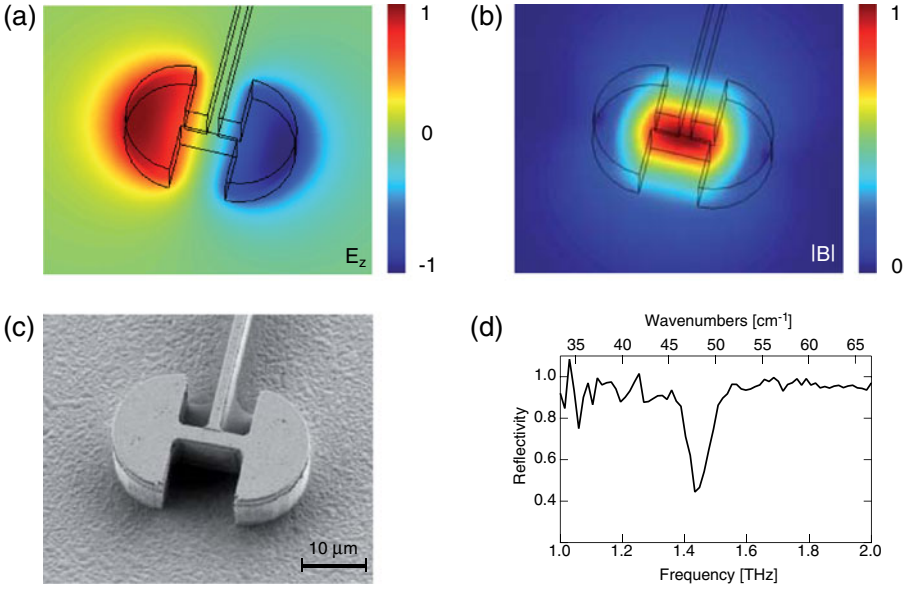

Fig. 2 Electric and magnetic field are separated in the cavity as seen in a finite element simulation shown in (**a**) for the electric and in (**b**) for the magnetic field. **c** shows an electron micrograph of an actual device. A typical absorption curve of a resonator array is seen in (**d**). The figure is adapted from [4]

2 LC-based Lasers

To provide the necessary gain for laser devices, a quantum cascade laser active region [17] can be inserted into the volume between the capacitor plates. The gain of the used design peaks at a frequency of 1.5 THz. Symmetric cavities with two half circular capacitors as shown in Fig. 2c, are used as they provide a natural ground in the middle of the inductance which is used for electrical pumping. Devices are fabricated by metallisation of the molecular beam epitaxy (MBE) grown 8 μm thick epitaxial layer, wafer bonding to a hosting substrate and removal of the original substrate. Then, the cavities are defined by optical lithography, top metallisation and dry etching. An isolation layer between the feeding line and the gain medium ensures that only the gain medium in the cavity is electrically pumped. For this geometry, a total quality factor $Q = 41$ is found in finite element simulations [4], determined by ohmic ($Q_{Ohm} = 53$) and radiative ($Q_{Rad} = 189$) losses. Using a Voigt fit, the lower $Q = 20$ found in a reflection measurement of an array of resonators in Fig. 2d is explained as the result of inhomogeneous broadening caused by lithographic variations.

Light-current-voltage characteristics are displayed in Fig. 3, which are adapted from [4]. At a current of ≈ 1.2 mA, a steep, super exponential increase in optical output power is observed in (a). Output power peaks at 80 pW for a current of 1.55 mA. Also, the linewidth decreases from 120 GHz to below the 7 GHz resolution limit of the spectrometer, suggesting operation close to threshold. Spectral narrowing of the emission with increasing injection current is also shown in Fig. 3b.

To clearly reach the lasing regime, a magnetic field is applied perpendicular to the quantum well plane restricting the electron dispersion to discrete Landau levels. This

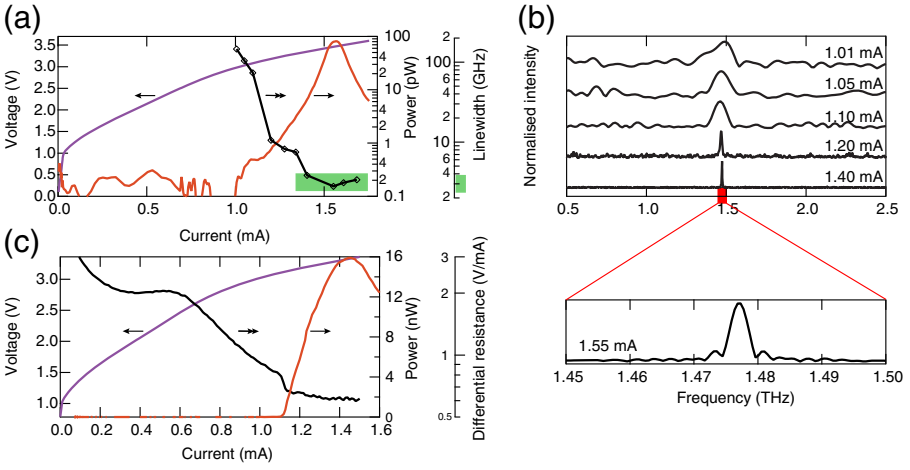

Fig. 3 The figure is adapted from [4]. Light-current-voltage characteristics of a single LC-cavity. Optical output power is detected with a He-cooled bolometer. Linewidth is determined with a FTIR-spectrometer and displayed in (**a**) and (**b**) as a function of current. **c** shows light-current-voltage characteristics of a device subjected to 2.3 T magnetic field. At the lasing threshold, the differential resistance drops abruptly

strongly affects intrasubband and intersubband transition lifetimes [18]. At a field of 2.3 T, the device shows a linear increase of optical emission power with current above lasing threshold of $\approx$ 1.1 mA as seen in Fig. 3c. This is accompanied by an abrupt drop in the differential resistance, also a clear sign of laser threshold. A maximum output power of 16 nW is reached.

A detailed study of the number of photons present in the cavity below and above threshold was conducted. The usual rate equation model for QC lasers was modified by including the effect of the microcavity on the spontaneous emission through the Purcell factor. The details of the calculation can be found in ref. [19]. Here we discuss the main conclusions which are represented in Fig. 4. The Purcell factor [20] is expressed as:

$$F_P = \frac{3Q(\lambda/n)^3}{4\pi^2 V}\Gamma \tag{1}$$

where Q is the quality factor of the lowest quality resonance (resonator or intersubband transition), λ is the emission wavelength, n is the mode refractive index, V is the active region volume and Γ is the mode overlap factor with the active region. For the LC laser cavity we obtain a theoretical $F_P = 17$.

By fitting the experimental data with a rate equation model, a Purcell factor of 25 ± 8 was deduced in fair agreement with the theoretical value.

In Fig. 4, we can see that the behavior of the LC laser is reproduced when microcavity effects, expressed through the Purcell factor, are taken into account.

The difficulty to achieve laser threshold at high temperatures constitutes a severe limitation for THz QC lasers. One possibility to circumvent this problem and realize semiconductor-based THz emitters is to work with LEDs rather than lasers and exploit microcavity characteristics such as the Purcell effect which, by changing the density of available photonic modes, can modify the spontaneous emission lifetime. This is especially attractive in the THz range, where spontaneous emission lifetimes

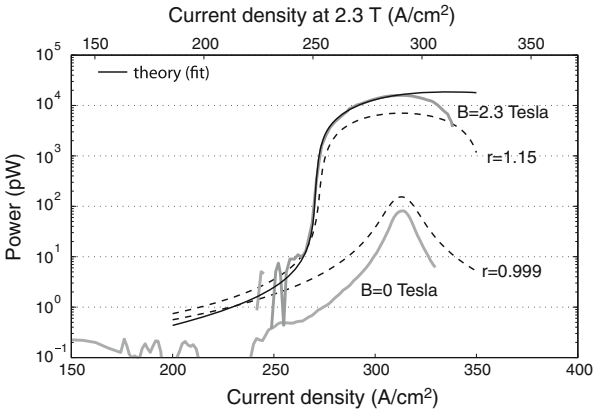

Fig. 4 The figure is adapted from [19]. *Thick grey lines* show experimental light-current characteristics without and with magnetic field. The *thin black line* is a fit using the measured Purcell factor. The fit is improved (*dashed lines*) when assuming that the population inversion ratio r is dominated by the detuning between the material gain and the cavity mode

are very long - on the order of μs. The ps time scale nonradiative intersubband mechanisms [21] are the main limitations. In the following section of the paper, we will discuss how the enhancement of the emission from an intersubband LED can be realized employing microcavities and driving the system in the strong light-matter coupling regime, as suggested in ref. [22].

3 LC-based Polariton Emitters

LC cavity based QC laser operation above threshold could so far only be demonstrated in the presence of a magnetic field, adding additional confinement to the electronic states. With lasers just reaching threshold, other classes of intersubband devices are of interest. In the same LC kind of microcavities, the interaction of the cavity field with a 2D electron gas can be strong enough to allow devices to enter the strong and ultra strong coupling regime [23] where new mixed light matter eigenstates - called intersubband polaritons [24] - characterise the optical properties.

In this kind of devices, Rabi frequencies of many hundred GHz can be reached, corresponding to an oscillation period on the order of the lifetime of an electronic intersubband excitation - typically a few picoseconds.

Such polaritonic resonances have been observed in reflection measurements [23, 25–27] and more recently electroluminescence from polaritonic states has also been observed [16]. Intersubband polariton electroluminescent devices based on resonant injection and multi mode cavities in the mid infrared range have already been demonstrated in 2008 [28–30].

In new experiments, we integrate semiconductor square quantum wells with intersubband transition frequencies in the THz range into a metamaterial where the sub-wavelength meta-atoms are constituted by LC resonators of the kind employed for the laser devices discussed above. A schematic of such a metasurface is shown in Fig. 5a.

The samples were MBE-grown in the GaAs/AlGaAs material system, with fifteen 27.8 nm wide quantum wells, totaling a sample thickness of 800 nm. The transition

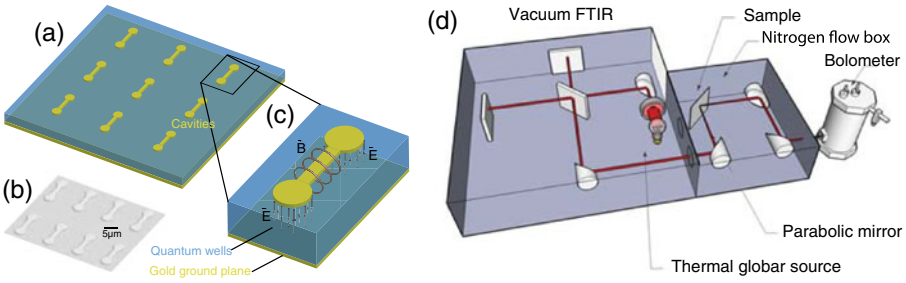

Fig. 5 **a** shows a schematic of the sample with an array of identical resonators. The cavities are deposited on top of the quantum wells, with a gold ground plane below. **b** is an electron micrograph of a part of a sample. The coupling and confinement of a single cavity is illustrated in (**c**). The electric field is to a large extent directed in the growth direction and therefore parallel to the dipole moment of the intersubband transition. **d** displays a schematic of the reflection measurement setup. **a–c** are adapted from [16]

frequency between the lowest subbands is $\omega_{ISB} = 3.9$ THz. After metallisation and wafer bonding to a hosting substrate, the original substrate was removed and the cavities were defined by optical lithography, metallisation and lift-off. Samples were cleaved into 1×1 mm sized pieces containing several hundred identical resonators and indium soldered to copper heat sinks. Fig. 5b shows an electron micrograph of a part of an actual sample. Part (c) illustrates how the electric field couples to the intersubband dipole moment in an individual cavity.

The optical properties are studied in reflection measurements in an interferometer with a Si-bolometer detector shown schematically in Fig. 5d. The beam path was partially evacuated and partially nitrogen purged.

The cavity mode is tuned lithographically. At a temperature of 10 K, we observe two distinct peaks in reflection spectra tuning with cavity resonance frequency. Spectra showing these upper and lower polaritons are shown in Fig. 6a. A clear anticrossing of the cavity mode and the intersubband transition line is observed and the Rabi frequency Ω_R is calculated to be 535 GHz at a relative coupling strength $\Omega_R/\omega_{ISB} = 0.13$ with a sheet carrier density of 0.7×10^{11} cm^{-2}. The experimental data is compared to a theoretical model [23] in Fig. 6b. The agreement with the model is good.

In square quantum wells, the coupling strength in terms of Rabi frequency is

$$\Omega_R = \sqrt{\frac{\pi e^2}{4\pi\epsilon_0 n^2 m^*} \frac{f_{12} N (N_1 - N_2)}{L}} \tag{2}$$

as pointed out in [23], where e is the electron charge, n is the mode refractive index, m^* is the effective electron mass, f_{12} is the oscillator strength, N is the number of quantum wells, N_x is the electron population in subband x and L is the cavity thickness. The Rabi frequency is proportional to the square root of the population difference between the two lowest subbands and therefore depends on the sample

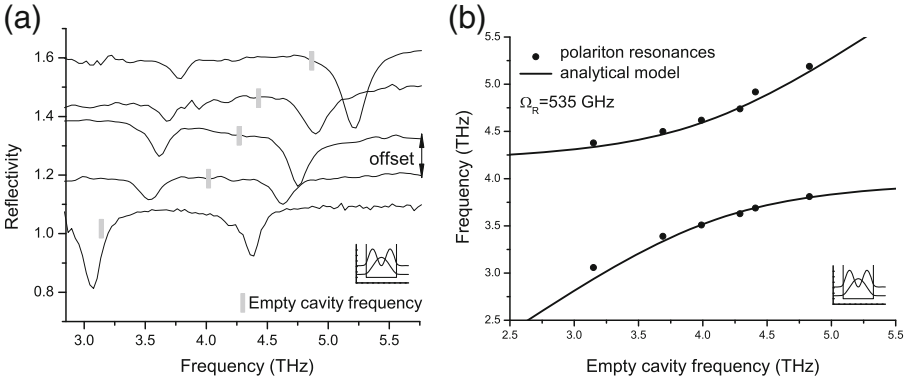

Fig. 6 **a** reflection spectra of samples with different cavity resonance frequencies. The respective empty cavity frequency is indicated as a *grey bar* for each sample. Two distinct polariton peaks are visible in each spectrum. They are anticrossing and tuning with cavity resonance frequency. **b** anticrossing curve comparing the measured polaritonic resonances (*dots*) to a model (*lines*)

temperature. We expect a decreasing coupling strength with increasing thermal population of the second subband at higher temperatures. This behaviour is observed and shown in Fig. 7. The studied sample is the one closest to the anticrossing point. The inset compares the expected Rabi frequency with the measured value in the reflection spectra. The calculated curve is based on the temperature dependent electronic populations of the two lowest subbands of the well as determined by a selfconsistent Schrödinger-Poisson calculation. At room temperature, the predicted $\Omega_R = 240$ GHz vanishes in a strongly broadened single resonance.

To overcome temperature limitations, similar experiments were performed with parabolic quantum wells coupled to the same kind of cavity [25, 27]. In parabolic quantum wells, all intersubband transitions contribute to the same intersubband line, making the observed transition frequency insensitive to the electron distribution and therefore to temperature. Another interesting property of parabolic quantum wells is, that a depolarisation shift [31], which is usually blueshifting an observable transition from the single electron transition in an empty well, is exactly compensated, leaving the transition unshifted. This effect is analogous to "Kohn's theorem", which makes similar predictions for inter Landau level transitions [32]. This allows maintaining a high ratio of the Rabi frequency to the intersubband transition frequency at large dopings, making these devices very interesting for ultra strong coupling and room temperature emission experiments. Effective parabolic potentials are achieved by digitally alloying GaAs and $Al_{1-x}Ga_xAs$.

In such samples, a Rabi frequency of up to 1.2 THz could be observed at an intersubband transition frequency of 4.5 THz, constituting a total splitting of the branches of more than half the quantum well transition energy. Resonance frequencies and coupling strengths remained constant from cryogenic to room temperature. The linewidths broaden though. Typical spectra are shown in Fig. 8a, which were acquired at cryogenic temperatures. In Fig. 9, the polaritonic spectra are compared to

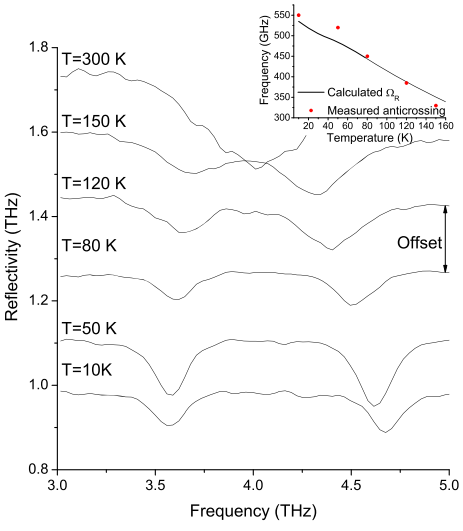

Fig. 7 Reflection spectra of a sample close to the anticrossing point at different temperatures. Coupling strength decreases with decreasing population difference. The inset compares the observed Rabi frequency to a theoretical prediction

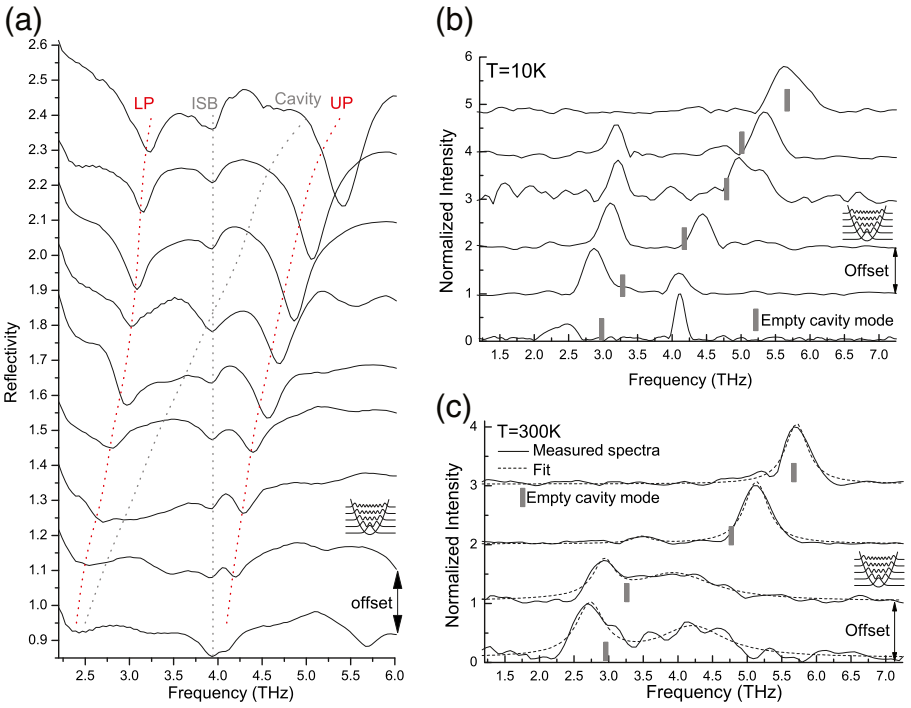

Fig. 8 **a** reflection spectra (T=10 K) of a sample containing eight modulation doped parabolic quantum wells. Two polaritonic resonances marked *LP* and *UP* are observed in each sample. The uncoupled intersubband transition is also visible and marked *ISB*. The empty cavity frequency of each sample is indicated by the *grey dotted line* marked *Cavity*. **a** is reprinted from [27]. Copyright (2012) by the American Physical Society. **b** electroluminescence from intersubband polariton states observed at low temperature (T=10 K). Two emission peaks in each spectrum correspond to the lower and upper polariton state. The empty cavity frequency is indicated in each spectrum. **c** displays electroluminescence observed at room temperature. The peaks are broadened but remain at the same frequencies when fitted with a double Lorentzian function. (**b**) and (**c**) are adapted from [16]

the same model as above for the experiments with square wells [26] and show good agreement. An Ω_R of 816 GHz is found for the displayed samples.

Exploiting the advantages of parabolic quantum wells, electroluminescence experiments using in plane excitation of the electron gas were done [16]. The samples were employing the same quantum wells studied above in reflection. In order to electrically insulate them from the gold ground plane, a nitride isolation layer was introduced between the quantum wells and the gold ground plane. As a result, the cavity volume is increased and Ω_R is reduced. Electrical contact to the electron gas was provided by Ge/Au contacts which were deposited on two opposing sides of the sample surface and annealed.

Electroluminescence spectra at cryogenic and room temperature are shown in Fig. 8b, c. The spectra show two anticrossing polaritonic peaks characterised by a Ω_R of 720 GHz. Both polaritonic resonances are visible in a wide range of empty cavity resonance frequencies, which are indicated in the figure as grey bars. Electroluminescence could be observed up to room temperature as shown in Fig. 8c. The lines

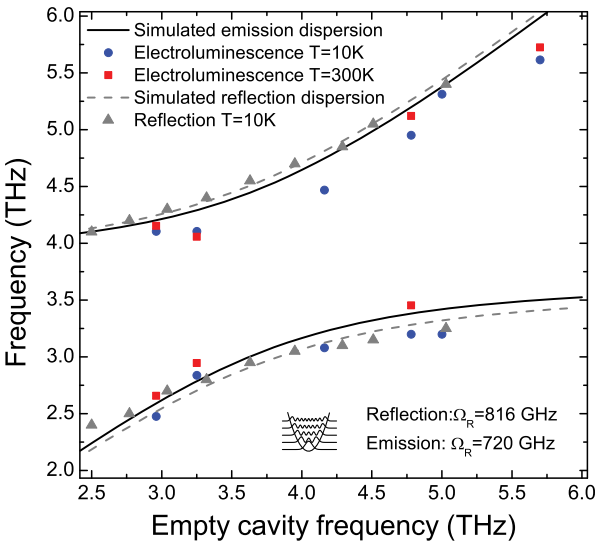

Fig. 9 Anticrossing curve of parabolic well samples. Reflection peaks (*grey triangles*) and simulation (*grey dashed line*) are shown together with the electruluminescence peaks (T=10 K: *blue circles*, T=300 K: *red squares*) and a corresponding simulation (*black continuous lines*). The emission spectra are characterized by a lower Rabi frequency as the cavity volume is increased due to the addition of a nitride isolation layer

are heavily broadened, but when fitted with a double Lorentzian curve, an essentially unshifted resonance frequency is observed compared to the cryogenic temperature data. This is illustrated in Fig. 9, where the polaritonic electroluminescence peaks are indicated as (blue) dots for $T = 10$ K and as (red) squares for room temperature. Peaks also align well with the (black) continuous line model prediction. Power levels on the order of 60 pW have been demonstrated at low temperatures (100 mW electrically injected power), with a degradation to ≈ 2 pW at room temperature. Promising approaches for power improvement include increase of pumping efficiency and lowering of the radiative quality factor of the cavities. While the observed powers are much lower than the powers achieved in e.g. difference frequency generation based devices [33], direct generation of THz light with electrical injection can still be interesting, e.g. for low dissipation and low threshold demands.

4 Conclusions

In this paper, we summarized research on the physics of intersubband transitions in the THz range in a sub wavelength microcavity environment. Laser action at 1.5 THz in a "circuit" cavity was demonstrated by inserting quantum cascade gain material between the capacitor plates of a resonant LC cavity. We evaluated the weak coupling (Purcell regime) characteristics for an LED and then continued to describe experiments still involving intersubband transitions in microcavities but without population inversion. The strong light matter coupling regime between LC cavities acting as

meta-atoms of a metamaterial and quantum wells was reviewed. The use of parabolic quantum wells allowed to demonstrate room temperature ultra strong light-matter coupling. Finally, THz emission in the ultrastrong coupling regime was discussed in the situation of electrical in-plane pumping.

Acknowledgments We would like to thank Fabrizio Castellano and Laurent Nevou for contributions to the original work. This work was supported by Swiss National Science Foundation through Contract No. 200020–129823/1.

References

1. B. Deveaud, *The Physics of Semiconductor Micro Cavities* (Wiley-VCH, 2007).
2. A. Kavokin, J. J. Baumberg, G. Malpuech, and F. Laussy, *Microcavities* (Oxford University Press, 2006).
3. A. Wallraff, D. I. Schuster, A. Blais, L. Frunzio, R.-S. Huang, J. Majer, S. Kumar, S. M. Girvin, and R. J. Schoelkopf, Nature **431**, 162 (2004).
4. C. Walther, G. Scalari, M. I. Amanti, M. Beck, and J. Faist, Science **327**, 1495 (2010).
5. B. S. Williams, Nature Photonics **1**, 517 (2007).
6. C. Ciuti, G. Bastard, and I. Carusotto, Phys. Rev. B **72**, 115303 (2005).
7. C. Ciuti and I. Carusotto, Phys. Rev. A **74**, 033811 (2006).
8. S. De Liberato, C. Ciuti, and I. Carusotto, Phys. Rev. Lett. **98**, 103602 (2007).
9. J. B. Pendry, A. J. Holden, D. J. Robbins, and W. J. Stewart, IEEE Trans. Microwave Theory and Tech. **11**, 2075 (1999).
10. G. Scalari, C. Maissen, D. Turcinkova, D. Hagenmuller, S. Liberato, C. Ciuti, C. Reichl, D. Schuh, W. Wegscheider, M. Beck, et al., Science **335**, 1323 (2012).
11. D. Dietze, A. Benz, G. Strasser, K. Unterrainer, and J. Darmo, Optics Express **19**, 13700 (2011).
12. E. Strupiechonski, G. Xu, M. Brekenfeld, Y. Todorov, N. Isac, A. M. Andrews, P. Klang, C. Sirtori, G. Strasser, A. Degiron, et al., Appl. Phys. Lett. **100**, 131113 (2012).
13. H. Park, S. Kim, S. Kwon, Y. Ju, J. Yang, J. Baek, S. Kim, and Y. Lee, Science **305**, 1444 (2004).
14. M. Hill, Y. Oei, B. Smalbrugge, Y. Zhu, T. Vries, P. Veldhoven, F. Otten, T. Eijkemans, J. Turkiewicz, H. Waardt, et al., Nat. Photonics **1**, 589 (2007).
15. Y. Chassagneux, J. Palomo, R. Colombelli, S. Dhillon, C. Sirtori, H. Beere, J. Alton, and D. Ritchie, Appl. Phys. Lett. **90**, 091113 (2007).
16. M. Geiser, G. Scalari, F. Castellano, M. Beck, and J. Faist, Appl. Phys. Lett. **101**, 141118 (2012).
17. C. Walther, M. Fischer, G. Scalari, R. Terazzi, N. Hoyler, and J. Faist, Appl. Phys. Lett. **91**, 131122 (2007).
18. G. Scalari, S. Blaser, J. Faist, H. Beere, E. Linfield, D. Ritchie, and G. Davies, Phys. Rev. Lett. **93**, 237403 (2004).
19. C. Walther, G. Scalari, M. Beck, and J. Faist, Opt. Lett. **36**, 2623 (2011).
20. E. M. Purcell, Physical Review **69**, 681+ (1946).
21. G. Scalari, C. Walther, M. Fischer, R. Terazzi, H. Beere, D. Ritchie, and J. Faist, Laser and Photonics Reviews **3**, 45 (2009).
22. R. Colombelli, C. Ciuti, Y. Chassagneux, and C. Sirtori, Semicond. Sci. Technol. **20**, 985 (2005).
23. Y. Todorov, A. M. Andrews, I. Sagnes, R. Colombelli, P. Klang, G. Strasser, and C. Sirtori, Phys. Rev. Lett. **102**, 186402 (2009).
24. D. Dini, R. Köhler, A. Tredicucci, G. Biasiol, and L. Sorba, Phys. Rev. Lett. **90**, 116401 (2003).
25. M. Geiser, C. Walther, G. Scalari, M. Beck, M. Fischer, L. Nevou, and J. Faist, Appl. Phys. Lett. **97**, 191107 (2010).
26. Y. Todorov, A. M. Andrews, R. Colombelli, S. De Liberato, C. Ciuti, P. Klang, G. Strasser, and C. Sirtori, Phys. Rev. Lett. **105**, 196402 (2010).
27. M. Geiser, F. Castellano, G. Scalari, M. Beck, L. Nevou, and J. Faist, Phys. Rev. Lett. **108**, 106402 (2012).
28. L. Sapienza, A. Vasanelli, R. Colombelli, C. Ciuti, Y. Chassagneux, C. Manquest, U. Gennser, and C. Sirtori, Phys. Rev. Lett. **100**, 136806 (2008).

29. A. Delteil, A. Vasanelli, P. Jouy, D. Barate, J. C. Moreno, R. Teissier, A. N. Baranov, and C. Sirtori, Phys. Rev. B **83**, 081404 (2011).
30. P. Jouy, A. Vasanelli, Y. Todorov, L. Sapienza, R. Colombelli, U. Gennser, and C. Sirtori, Phys. Rev. B **82**, 045322 (2010).
31. T. Ando, A. Fowler, and F. Stern, Rev. Mod. Phys. **54**, 437 (1982).
32. W. Kohn, Physical Review **123**, 1242 (1961).
33. K. Vijayraghavan, R. W. Adams, A. Vizbaras, M. Jang, C. Grasse, G. Boehm, M. C. Amann, and M. A. Belkin, Appl. Phys. Lett. **100**, 251104 (2012).